Adiabatic Rapid Passage for State Transfer and Sideband Cooling in an ^{87}Sr Optical Lattice Clock

Jia-An Li(李家安)[1,2,3], Jin Cao(曹进)[1,3,†], Chao-Zhe Hu(胡超哲)[1,2,3], Wei Tan(谭巍)[1,2,3], Jing-Jing Xia(夏京京)[1,3], Yan-Yan Liu(刘艳艳)[1,3], Chi-Hua Zhou(周驰华)[1,2,3,††], and Hong Chang(常宏)[1,2,3,†††]

[1]National Time Service Center, Chinese Academy of Sciences, Xi' an 710600, China

[2]School of Astronomy and Space Science, University of Chinese Academy of Sciences, Beijing 100049, China

[3]Hefei National Laboratory, University of Science and Technology of China, Hefei 230088, China

[†]Corresponding authors. E-mail: caojinaha@qq.com

[††]Corresponding authors. E-mail: zhouchihua@ntsc.ac.cn

[†††]Corresponding authors. E-mail: changhong@ntsc.ac.cn

Abstract

Efficient population transfer and motional state control are important for optical lattice clocks and precision experiments with lattice-trapped neutral atoms. Here we experimentally investigate adiabatic rapid passage (ARP) on the clock transition of a one-dimensional ^{87}Sr optical lattice clock and develop a mode-resolved model for ARP on motional sidebands. On the carrier transition, ARP enables robust internal-state transfer with a maximum excitation fraction of 0.98(2). On the blue motional sideband, ARP increases the maximum excitation fraction from 0.47(2) to 0.55(3), and the measured dynamics are consistently reproduced by the mode-resolved model. The model further predicts that the sideband transfer efficiency can exceed 0.88 when the carrier Rabi frequency is increased to 15 kHz. Applying ARP to the red-sideband cooling reduces the axial mean vibrational occupation to approximately 0.038, corresponding to a motional ground-state population of 0.96. These results provide a quantitative basis for designing ARP excitation on motional sidebands and for optimizing sideband cooling in lattice-trapped atoms, with direct relevance to coherent state preparation in optical lattice clocks and related precision-measurement experiments in neutral atoms.

Keywords: optical lattice clock, adiabatic rapid passage, motional sideband, sideband cooling
PACS: 06.30.Ft; 37.10.Jk; 37.10.De; 42.50.Gy

1. Introduction

Optical lattice clocks based on neutral atoms have reached high levels of frequency stability and accuracy, [1–4] enabling applications in tests of fundamental physics [5–8] and relativistic geodesy. [9–12] In these clocks, thousands of atoms are trapped in a magic wavelength optical lattice and interrogated on the ultranarrow $^1S_0 \rightarrow {}^3P_0$ clock transition. Efficient excitation of the clock transition and control of the external motion are therefore central to high-contrast clock interrogation, reproducible state preparation, and precision measurements with lattice-trapped atoms. In typical operation, coherent excitation of the clock transition is driven by resonant π pulses, [13] which are sensitive to laser intensity fluctuations, detuning errors, and the spatial inhomogeneity of the Rabi frequency. [14,15] These effects remain relevant for the lattice-trapped atoms with finite temperature, where several motional states can be populated even in the Lamb-Dicke regime. The motional distribution produces a spread of effective Rabi frequencies on

the carrier transition and a spread of resonance frequencies and sideband couplings for motional sidebands. Therefore, coherent transfer and sideband cooling can be degraded by motional inhomogeneity.

Adiabatic rapid passage (ARP) provides a promising route to mitigate these limitations. [16–20] In ARP, the laser frequency is swept through resonance, and population transfer occurs when the system follows the instantaneous dressed state under the adiabatic condition. Compared with fixed frequency excitation, ARP can be more tolerant of resonance offsets and variations in coupling strength. [21–23] ARP has been used in nuclear magnetic resonance, [24] Rydberg systems, [25–28] and several optical clock platforms. [29–31] For the carrier transition in an optical lattice clock, the motional quantum number is conserved, and the excitation can often be described by an effective Landau-Zener picture with corrections from finite coherence and loss processes. How ARP behaves on motional sidebands is less well established.

To describe ARP on motional sidebands in a thermal lattice-trapped ensemble, we develop a mode-resolved treatment in which each thermally populated motional component (n_z, n_r) is assigned its own sideband resonance frequency and Rabi coupling. The resonance frequency is determined by the axial trap anharmonicity and the coupling between axial and radial motion, while the sideband Rabi frequency is determined by the corresponding motional-state-dependent transition matrix element. The dynamics of each motional component are then propagated separately during the frequency sweep and thermally averaged to obtain the observable excitation.

This mode-resolved description provides access to information that is lost when the ensemble is replaced by a single effective two-level transition. In particular, different motional components cross resonance at different times during the same sweep and experience different coupling strengths, so their adiabaticity conditions are not identical. A single effective Rabi frequency therefore cannot fully represent the distribution of resonance-crossing times and transfer probabilities across the thermal ensemble. The mode-resolved model makes it possible to identify which motional components remain weakly transferred, to determine how the thermal distribution limits the attainable sideband excitation, and to quantitatively optimize the sweep bandwidth, sweep duration, and coupling strength.

In this work, we investigate ARP on the carrier and motional sidebands of a one-dimensional ^{87}Sr optical lattice clock. We first characterize carrier ARP and compare it with fixed frequency Rabi excitation under the same experimental conditions. We then calculate the sideband spectrum and sideband Rabi coupling for atoms trapped in the optical lattice and compare the calculated blue sideband ARP dynamics with the measured results. Finally, we apply red sideband ARP to axial sideband cooling. The carrier ARP reaches an excitation fraction of 0.98(2), while the blue sideband measurement tests the mode-resolved calculation and identifies the finite sideband Rabi frequency relative to the sweep bandwidth as the main limitation under the present conditions. Red-sideband ARP cooling reduces the axial mean vibrational occupation to $\bar{n}_z = 0.038$, corresponding to a motional ground-state population of $p_0 = 0.96$. These results provide quantitative guidance for choosing sweep parameters and Rabi frequencies in sideband excitation and cooling of optical lattice clocks.

2. Experimental system and ARP implementation

The experiment is performed with a one-dimensional fermionic ^{87}Sr optical lattice clock. The overall experimental layout and the radio frequency control setup used for pulse interrogation at fixed frequency and with ARP are shown schematically in Fig. 1. Each experimental cycle begins with laser cooling in two stages in the $^1S_0 \rightarrow {}^1P_1$ transition at 461 nm and the narrow $^1S_0 \rightarrow {}^3P_1$ transition at 689 nm.

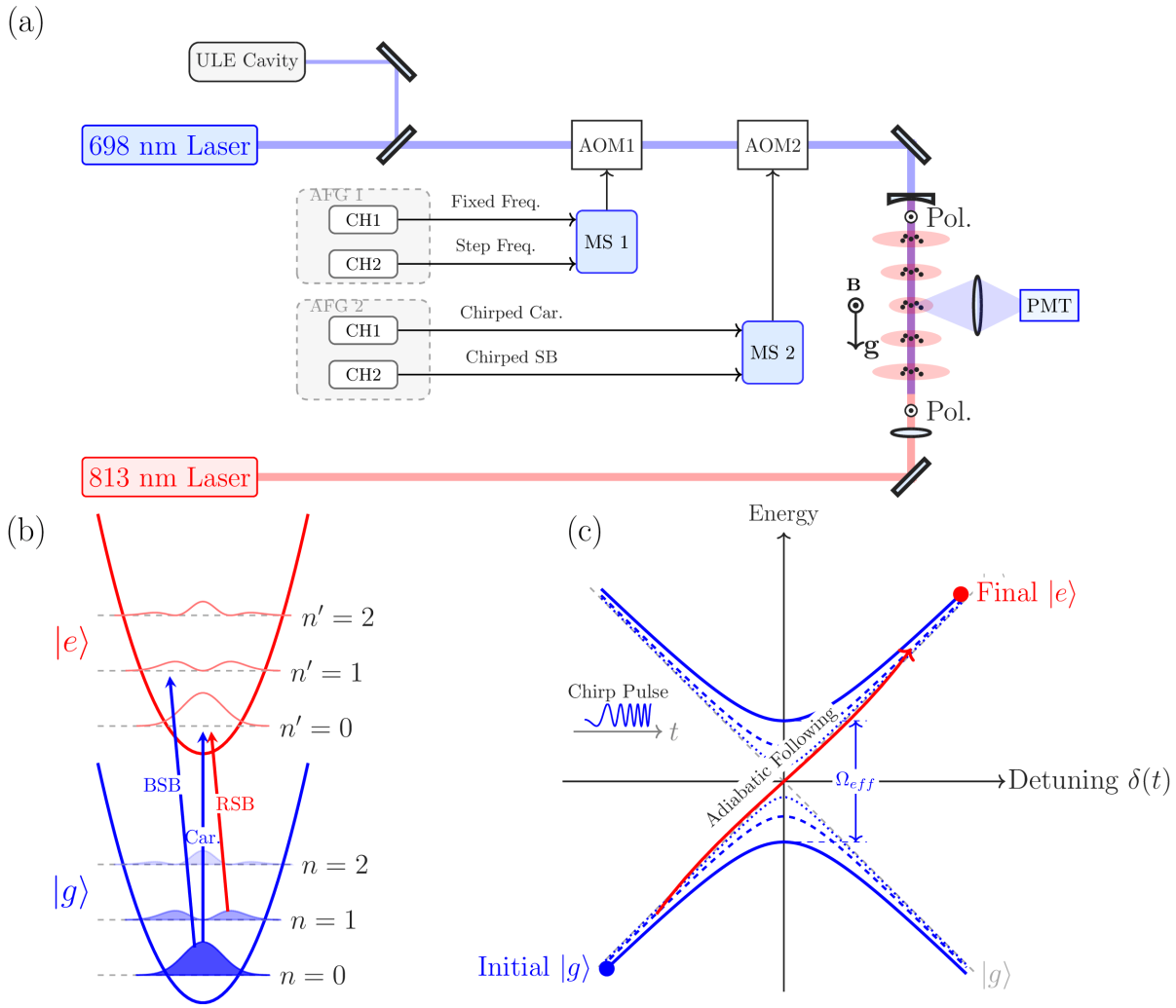


Fig. 1. (a) Schematic of the ^{87}Sr optical lattice clock and the radio-frequency control chain used for clock interrogation. AOM: acousto-optic modulator, ULE: ultra low expansion, MS: microwave switch, AFG: arbitrary function generator, PMT: photomultiplier tube. (b) Relevant internal and axial motional states in the lattice. The carrier transition couples $|g, n\rangle$ to $|e, n\rangle$, while the red and blue motional sidebands couple $|g, n\rangle$ to $|e, n-1\rangle$ and $|e, n+1\rangle$, respectively. (c) Dressed state picture of ARP. A chirped detuning $\delta(t)$ sweeps through the resonance, and adiabatic following transfers population when the sweep rate is sufficiently slow compared with the square of the coupling strength.

Approximately 10^4 atoms are then loaded into a vertically oriented one-dimensional optical lattice operating near the magic wavelength of 813.4 nm. The lattice beam is retroreflected to form a standing wave. For the measurements reported here, the axial trap frequency is obtained from the motional-sideband spectrum, yielding $\nu_z \simeq 59.5$ kHz. Within the harmonic approximation near the center of the Gaussian standing-wave lattice, the axial and radial trap frequencies are given by

$$\begin{aligned} \nu_z &= \frac{2}{h}\sqrt{U_0 E_r}, \\ \nu_r &= \frac{1}{\pi w_0}\sqrt{\frac{U_0}{m}} = \frac{\lambda_l}{\sqrt{2}\pi w_0}\nu_z, \end{aligned} \tag{1}$$

where U_0 is the peak lattice depth, $E_r = h^2/(2m\lambda_l^2)$ is the lattice photon recoil energy, m is the atomic mass, λ_l is the lattice wavelength, and w_0 is the $1/e^2$ intensity radius of the lattice beam. Using $\lambda_l =$ 813.4 nm and $w_0 \simeq 60$ μm, the measured axial trap frequency corresponds to $U_0 \simeq 73.5E_r$ and gives $\nu_r \simeq 181.6$ Hz.

For clock excitation, the axial Lamb–Dicke parameter is

$$\eta_z = k_p \cos\theta \sqrt{\frac{\hbar}{2m\omega_z}} \simeq \sqrt{\frac{h}{2m\lambda_p^2\nu_z}}, \tag{2}$$

where $k_p = 2\pi/\lambda_p$, $\omega_z = 2\pi\nu_z$, and θ is the angle between the clock beam and the lattice axis. For the nearly axial clock beam used here, $\theta \simeq 0$, and the probe wavelength $\lambda_p = 698$ nm gives $\eta_z \simeq 0.281$.

After loading, the atoms are spin polarized to the stretched Zeeman sublevel $m_F = +9/2$ of the ground state $^1S_0$, which defines the internal state $|g\rangle$. The external motional state remains thermally distributed. From the measured axial temperature $T_z \simeq 1.8$ µK, the initial axial mean vibrational quantum number is estimated to be $\bar{n}_z \simeq 0.26$, corresponding to an axial ground-state population of approximately 0.79 based on a thermal distribution $p_0 = 1/(1 + \bar{n}_z)$. The radial temperature is about $T_r \simeq 4.82\,\mu$K.

The clock transition $^1S_0 \rightarrow {}^3P_0$ at 698 nm is interrogated using a laser prestabilized to a high-finesse ULE cavity. The clock beam is aligned along the lattice axis. Phase coherent control of the pulse frequency and duration is implemented with two cascaded acousto-optic modulators driven by arbitrary function generators and microwave switches. Fixed-frequency pulses and chirped ARP pulses are generated by independent radio frequency sources and are triggered by digital timing electronics. Under the present experimental conditions, the maximum carrier Rabi frequency is $\Omega_c/2\pi =$ Hz. The excitation fraction after the interrogation sequence is measured by electron shelving detection and normalized as:

$$P_e = \frac{N_e - N_{bg}}{N_g + N_e - 2N_{bg}}, \tag{3}$$

where N_g and N_e are the atom numbers detected in the ground and excited clock states, and N_{bg} represents the detected background noise.

For an ARP pulse, the laser frequency is swept linearly according to

$$f(t) = f_\mathrm{i} + \frac{f_\mathrm{f} - f_\mathrm{i}}{T_\mathrm{sw}} t, \qquad 0 \le t \le T_\mathrm{sw}, \tag{4}$$

where f_i and f_f are the initial and final frequencies, respectively, and T_sw is the sweep duration. The sweep span and center frequency are defined as

$$\Delta f_\mathrm{sw} = |f_\mathrm{f} - f_\mathrm{i}|, \qquad f_\mathrm{c} = \frac{f_\mathrm{i} + f_\mathrm{f}}{2}. \tag{5}$$

All ARP sweeps used in this work proceed from high to low frequency, with $f_f < f_i$. The initial frequency, final frequency, and sweep duration are independently programmed using the arbitrary function generator, and the frequency interval is selected separately for the carrier and each resolved motional sideband. For the measurements in which T_sw is varied, including the carrier, blue-sideband, and red-sideband duration scans, f_i and f_f are held fixed. Consequently, both Δf_sw and f_c remain constant. By contrast, in the blue-sideband sweep span measurement described in Appendix B.3, T_sw and f_i are fixed while f_f is varied toward the carrier. Thus, both Δf_sw and f_c vary in that measurement.

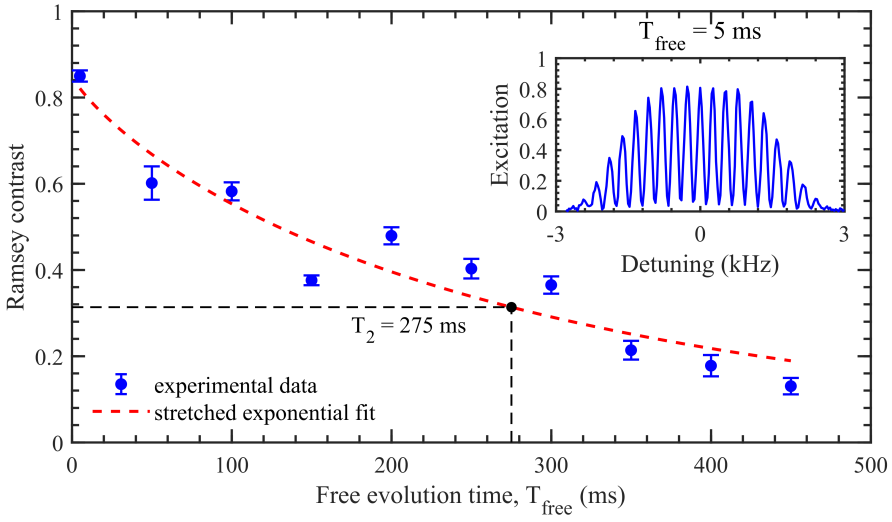


Fig. 2. coherence measurement of the clock transition in the lattice trapped ensemble. The dashed line is a fit to a stretched exponential decay, yielding $T_2 \simeq 275$ ms, $C_0 = 0.806$, and $\beta = 0.832$. Each point is obtained from 20 independent measurements, and the error bars denote the standard error of the mean.

3. Results and Discussion

3.1. Carrier ARP in the lattice-trapped ensemble

The carrier couples $|g, n\rangle$ to $|e, n\rangle$ without changing the axial vibrational quantum number. Compared with motional sideband transitions, the carrier transition can be treated as a simpler frequency swept transfer between the two clock states. We first characterize the coherence time of the clock transition in the lattice-trapped ensemble by Ramsey spectroscopy. Two resonant $\pi/2$ pulses are applied with a variable free evolution time T_{free}, and the Ramsey contrast is extracted from the peak-to-peak excitation signal. For each value of T_{free}, the measurement is repeated 20 times, and the error bars in Fig. 2 denote the standard error of the mean. The contrast decay is fitted with a stretched exponential function: [32]

$$C(T_{\text{free}}) = C_0 \exp\left[-\left(T_{\text{free}}/T_2\right)^{\beta}\right], \tag{6}$$

where C_0 is the initial contrast, T_2 is the effective inhomogeneous coherence time, and β accounts for the non-exponential decay of the ensemble coherence. The fit gives $T_2 \simeq 275$ ms, with $C_0 = 0.806$ and $\beta = 0.832$. For the carrier ARP measurement, the laser frequency is swept linearly across the carrier resonance with a fixed sweep span of $\Delta f_{\text{sw}} = 12$ kHz. This range covers the observed carrier resonance and residual detuning fluctuations while remaining much smaller than the axial trap frequency. The sweep duration T_{sw} is then varied to control the adiabaticity of the passage.

The measured excitation dynamics are shown in Fig. 3. As T_{sw} increases from the nonadiabatic short pulse regime, the excitation fraction increases rapidly and exceeds 0.9 at about 10 ms. It reaches a maximum value of 0.98(2) at intermediate sweep durations. For comparison, fixed-frequency Rabi driving under the same experimental conditions gives a lower maximum excitation fraction of 0.76(1), as shown in Appendix A.1. The excitation fraction remains between about 0.95 and 0.98 for sweep durations from approximately 15 ms to 70 ms. For longer sweeps, the excitation decreases slightly, reaching about 0.95 at the longest measured sweep duration near 90 ms.

The solid curve in Fig. 3 represents a fit using the effective Landau-Zener model described in Ap-

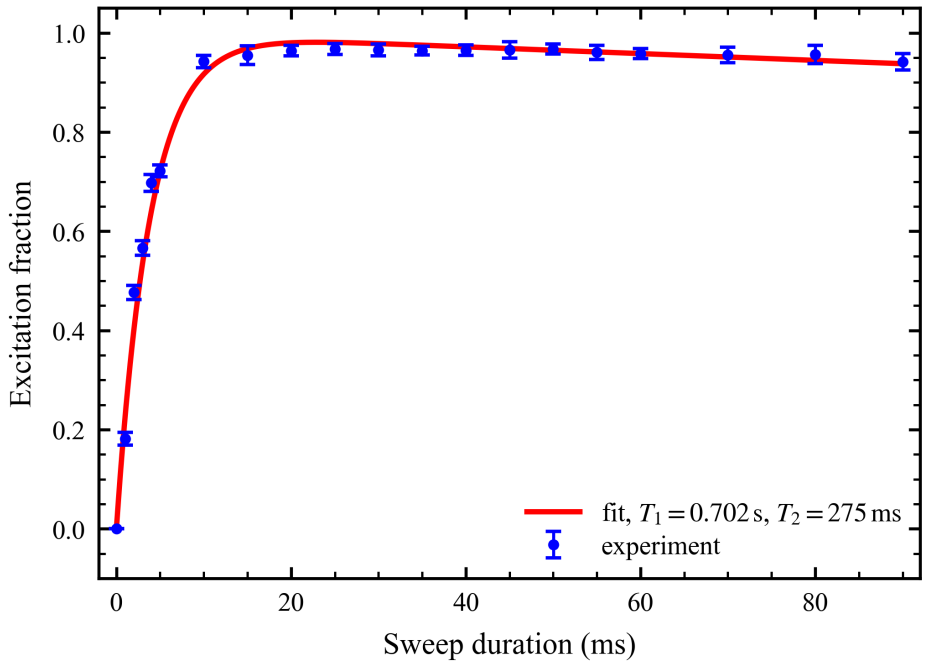


Fig. 3. Carrier excitation dynamics under ARP. The laser frequency is swept across the carrier transition with a fixed sweep span of $\Delta f_{\mathrm{sw}} = 12$ kHz. Blue points denote the measured final excited state probability. The red solid curve is a fit using the effective Landau-Zener model described in Appendix A.2, with $T_2 = 275$ ms and $T_1 = 0.702$ s. Error bars denote the standard error of the mean from 20 measurements.

pendix A.2. In this model, the ideal Landau-Zener transfer probability is modified by the independently measured coherence time T_2 and an effective survival factor T_1 that accounts for the reduction of the measured excitation during longer sweeps. The carrier Rabi frequency and sweep range are fixed at $\Omega_{\mathrm{eff}}/2\pi = 669$ Hz and $\Delta f_{\mathrm{sw}} = 12$ kHz, respectively, and T_2 is fixed at 275 ms. With T_1 as the only fitted dynamical parameter, the fit gives $T_1 = 0.702$ s. Here, T_1 should be understood as a phenomenological longitudinal relaxation time accounts for slow population loss or redistribution during the chirped interrogation, including possible contributions from atom loss, off-resonant scattering, heating-induced loss, and other technical relaxation processes. The agreement with the measured data shows that the carrier ARP under the present conditions is well captured by an effective Landau-Zener description with finite coherence and survival corrections. [18,23,30]

3.2. Blue sideband ARP with mode-resolved modeling

Compared with the carrier transition, the blue sideband is more difficult to drive efficiently because its coupling is reduced by the Lamb-Dicke factor and depends on the motional quantum numbers. The measured initial radial temperature $T_r \simeq 4.82$ μK corresponds to a broad distribution of radial motional states. Through axial-radial coupling, different radial components have different blue-sideband resonance frequencies and therefore cross resonance at different times during the same ARP sweep. The sideband coupling strengths also exhibit a radial-state dependence. The residual radial excitation thus produces inhomogeneous sideband broadening and nonuniform transfer efficiencies, making a single-mode Landau-Zener description insufficient for the blue-sideband ARP dynamics.

To describe the blue-sideband dynamics, we use the mode-resolved model developed in Appendix

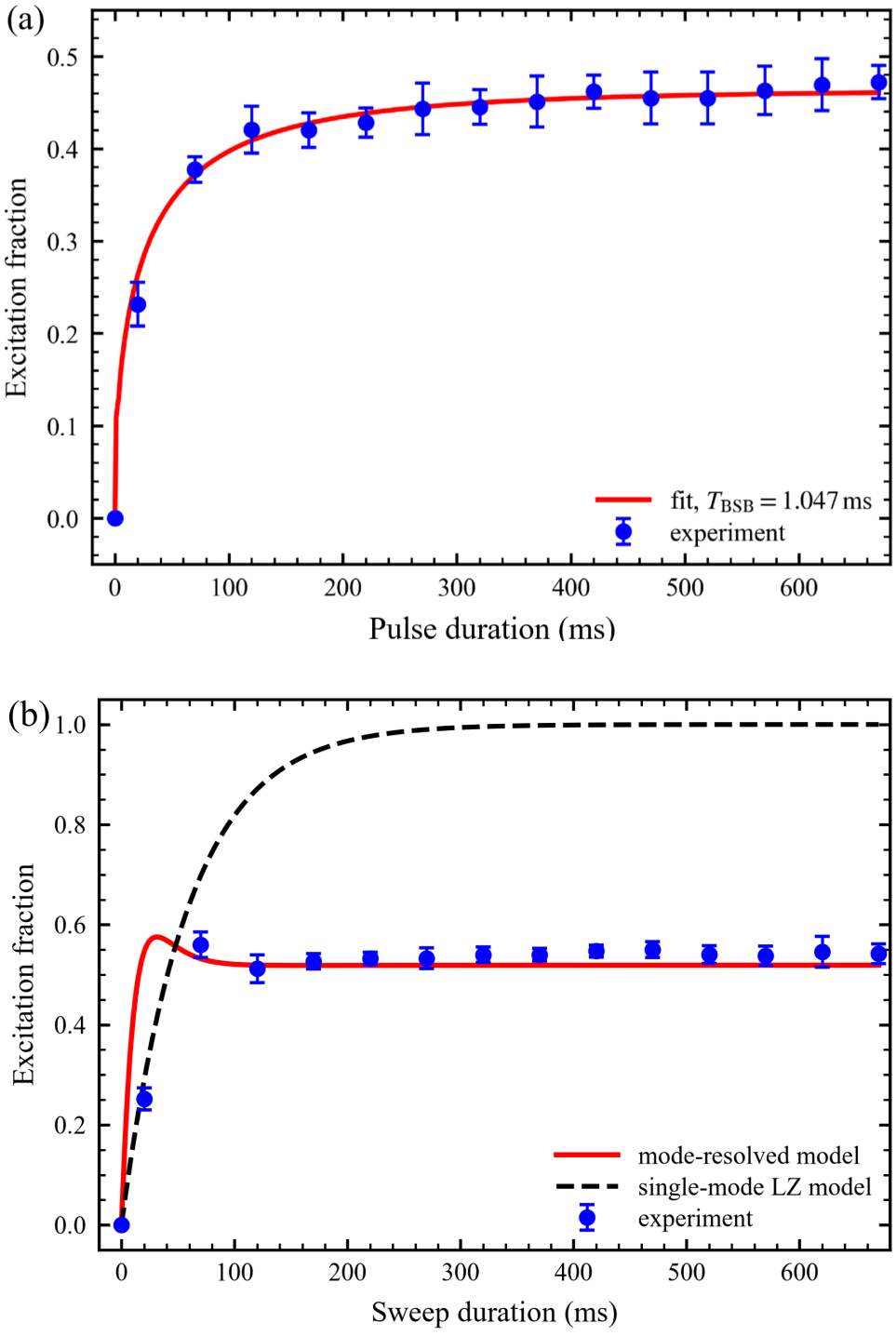


Fig. 4. Blue sideband excitation under fixed frequency driving and ARP. (a) Fixed frequency excitation near the blue sideband resonance as a function of pulse duration. The solid curve is a fit using the mode resolved sideband calculation described in Appendix B.2, yielding $T_{\mathrm{BSB}} = 1.047$ ms. (b) Blue sideband ARP with a fixed sweep span of $\Delta f_{\mathrm{sw}} = 15$ kHz. The blue solid curve is calculated using the mode-resolved model under the calibrated sideband parameters from (a), with the fixed detuning replaced by the time dependent chirped detuning. The black dashed curve is the result of the single-mode Landau–Zener model under the same parameters. ARP increases the maximum excitation fraction from 0.47(2) to 0.55(3). Error bars denote the standard error of the mean from 20 measurements.

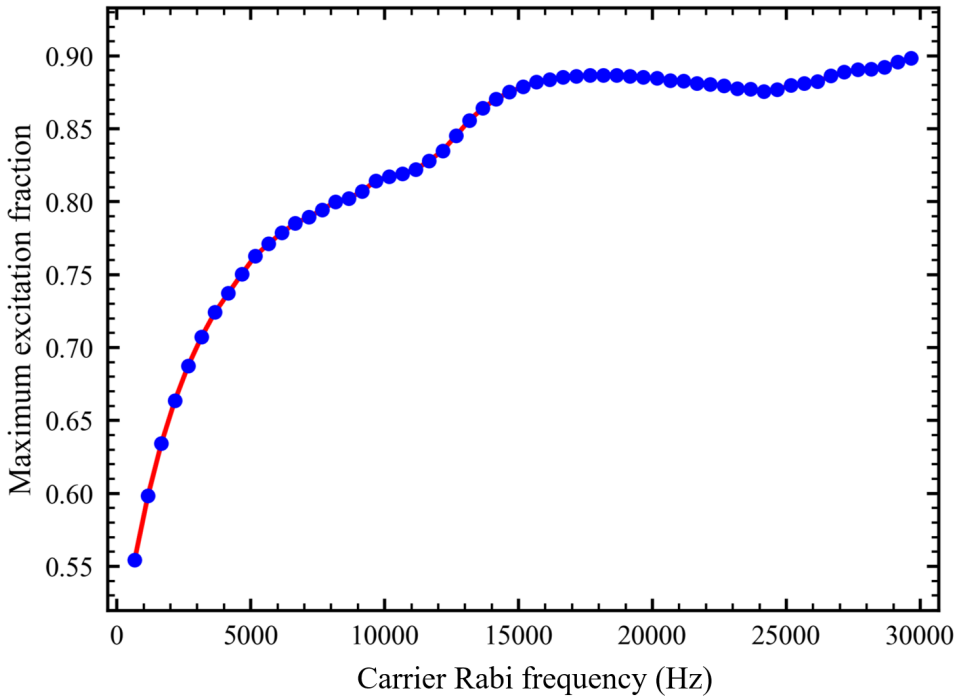


Fig. 5. Calculated maximum population transfer efficiency of blue sideband ARP as a function of the carrier Rabi frequency. For each carrier Rabi frequency, the calculation is performed over a range of sweep durations, and the largest final excitation fraction is retained. The sweep span is fixed at $\Delta f_{\mathrm{sw}} = 15$ kHz, while all other model parameters are kept at the values used for the present experimental conditions.

B.1–Appendix B.3. Unlike the single-mode Landau–Zener description, which predicts an excitation probability approaching unity for sufficiently slow sweeps, the mode-resolved calculation accounts for the distribution of resonance frequencies and coupling strengths among different motional states and reproduces the experimentally observed saturation of the sideband transfer efficiency. Each occupied motional component (n_z, n_r) is assigned its own blue-sideband resonance frequency $\gamma_{\mathrm{b}}(n_z, n_r)$ and sideband Rabi frequency $\Omega_{\mathrm{b}}(n_z, n_r)$. The thermal weights are determined from the measured axial and radial temperatures, $T_z \simeq 1.8$ μK and $T_r \simeq 4.82$ μK, respectively. The observed excitation is obtained by propagating each motional component separately and averaging the resulting transition probabilities over the thermal distribution. For the present carrier Rabi frequency $\Omega_{\mathrm{c}}^{\mathrm{eff}}/2\pi = 669(7)$ Hz, the thermally averaged blue-sideband Rabi frequency is approximately $\Omega_{\mathrm{b}}^{\mathrm{eff}}/2\pi = 161(2)$ Hz.

We first measure the excitation of the blue sideband under fixed-frequency driving, as shown in Fig. 4(a). The clock laser is tuned near the blue sideband resonance, and the pulse duration is varied. The maximum excitation fraction reaches 0.47(2). The solid curve is a fit to the measured excitation data using the mode-resolved model developed in the Appendix B.2. The fit gives an effective sideband dephasing time of $T_{\mathrm{BSB}} = 1.047$ ms, which characterizes the damping of the blue-sideband excitation during fixed-frequency driving and is used as the dephasing input for the ARP calculation below. This parameter represents residual transverse decoherence mechanisms that are not explicitly resolved in the mode-resolved Hamiltonian, including contributions from clock-laser frequency noise, magnetic-field-induced detuning fluctuations, and spatially inhomogeneous differential light shifts or probe intensities. Since the (n_z, n_r)-dependent sideband resonance frequencies and Rabi couplings are already explicitly included in the model, T_{BSB} primarily accounts for additional dephasing beyond the modeled motional-state inhomogeneity.

We then measure ARP on the blue sideband by sweeping the laser frequency linearly across the blue sideband resonance. In the Appendix B.3, as shown in Fig. 8, the excitation fraction increases with the sweep span and reaches a plateau at approximately 15 kHz. We then set the sweep span fixed at $\Delta f_{\mathrm{sw}} = 15$ kHz, which covers the main blue sideband feature while remaining separated from the carrier transition. As shown in Fig. 4(b), the red solid curve is calculated from the mode-resolved model, and the black dashed curve from the single-mode Landau–Zener model. The mode-resolved model gives an excitation fraction that increases with T_{sw} and reaches 0.55(3) at a sweep duration of about 70 ms, reproducing both the rise and the saturation of the measured blue sideband ARP excitation. By contrast, the single-mode Landau–Zener model predicts an excitation fraction approaching unity, which deviates significantly from the experimental data. These results indicate that the finite sideband Rabi frequency, the distribution of sideband resonance frequencies, and the effective dephasing time together determine the observed ARP dynamics, whereas the single-mode Landau–Zener model is no longer applicable to the sideband.

Under the present experimental conditions, ARP increases the maximum blue-sideband excitation fraction from 0.47(2) to 0.55(3). The improvement is mainly limited by the weak sideband coupling and the finite effective sideband dephasing time. To examine the dependence on coupling strength, the calculation is repeated for different carrier Rabi frequencies. For each carrier Rabi frequency, the sweep duration is varied and the largest final excitation fraction is retained, while all other model parameters are held fixed. As shown in Fig. 5, the calculated maximum excitation fraction exceeds 0.88 when the carrier Rabi frequency reaches 15 kHz. Since the available probe power limits the carrier Rabi frequency in the present experiment to 669(7) Hz Hz, the prediction at 15 kHz should be regarded as an idealized model extrapolation beyond the experimentally tested range. High-power narrow-linewidth 698 nm laser systems provide a practical route to the predicted regime. At higher Rabi frequencies, the sweep span and duration must be reoptimized for the increased sideband coupling.

.

3.3. Axial sideband cooling with red sideband ARP

The blue sideband results show that a chirped pulse can drive sideband excitation over a broader range of motional states than a fixed-frequency pulse. We therefore apply the same frequency swept approach to the red sideband for axial sideband cooling. Because axial-radial coupling produces comparable frequency broadening on the red and blue sidebands, the red-sideband sweep span is also set to $\Delta f_{\mathrm{sw}} = 15$ kHz. As shown in Fig. 6(a), the red sideband ARP excitation reaches a maximum of 0.19(1) at a sweep duration of about 270 ms. This value should be compared with the initial population outside the axial motional ground state, because the atoms initially in $n_z = 0$ are not coupled by the red sideband. With $p_0 = 0.79$, the participating fraction is $1 - p_0 \simeq 0.21$, and the observed maximum excitation corresponds to an effective transfer efficiency of approximately $0.19/(1 - p_0) \simeq 0.9$ for atoms initially occupying $n_z > 0$.

Based on this result, we implement axial sideband cooling using red sideband ARP. Each cooling cycle consists of a 270 ms red sideband ARP pulse followed by a 10 ms repumping stage, during which the 679 nm and 707 nm repumping lasers are applied simultaneously. To choose the number of cooling cycles, we measured the final mean axial occupation as a function of the cycle number, as shown in Fig. 6(b). The occupation decreases rapidly during the first several cycles and then approaches saturation after about ten cycles. We therefore used ten ARP cooling cycles for the final cooling measurement , corresponding to a total cooling time of 2.8 s. For comparison, conventional fixed frequency sideband cooling is applied continuously for the same total duration of 2.8 s. The 698 nm laser is fixed at an

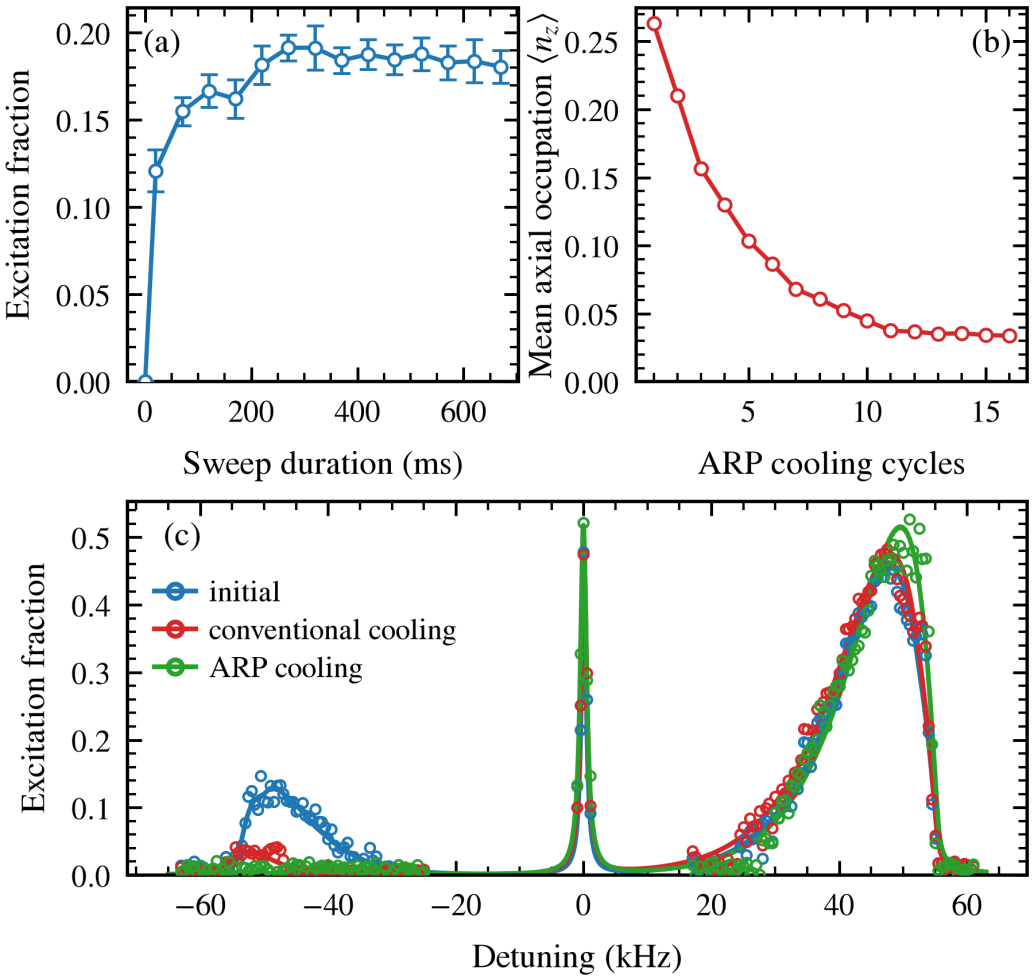


Fig. 6. Red sideband ARP and axial sideband cooling. (a) Red sideband ARP excitation with a fixed sweep span of $\Delta f_{\mathrm{sw}} = 15$ kHz. The excitation fraction reaches 0.19(1) at a sweep duration of about 270 ms. Error bars denote the standard error of the mean from 20 measurements. (b) Mean axial vibrational occupation after ARP cooling as a function of cooling cycle number. Each point is obtained from a single experimental measurement and is used to guide the choice of ten cooling cycles. (c) Motional sideband spectra of the initial ensemble, the ensemble after continuous fixed frequency sideband cooling for 2.8 s, and the ensemble after ten ARP cooling cycles with the same total cooling time. Sideband thermometry gives $T_z = 1.8$ μK and $p_0 = 0.79$ initially, $T_z = 1.2$ μK and $p_0 = 0.91$ after fixed frequency cooling, and $T_z = 0.86(9)$ μK, $\bar{n}_z = 0.038(13)$, and $p_0 = 0.963(13)$ after ARP cooling. The uncertainties for the ensemble cooled by ARP are the standard errors of the means from 20 independent sideband measurements.

experimentally optimized detuning of 50 kHz from the carrier, corresponding to the maximum of the measured red sideband excitation spectrum, while the 679 nm and 707 nm repumping lasers remain on throughout the cooling period. The 698 nm laser intensity, repumping laser intensities, initial atomic preparation, and lattice parameters are kept unchanged.

The final motional state is characterized by sideband thermometry. Fig.6(c) compares the red and blue sideband spectra of the initial ensemble, the ensemble after continuous fixed frequency sideband cooling, and the ensemble after ten ARP cooling cycles. After subtracting a constant background, the red and blue sideband areas are obtained by numerical integration. No specific line-shape function is assumed

in the extraction of the axial temperature. For a thermal axial distribution, the ratio $R = A_{\mathrm{RSB}}/A_{\mathrm{BSB}}$ gives [33–35]

$$\bar{n}_z = \frac{R}{1-R}, \qquad p_0 = \frac{1}{1+\bar{n}_z}, \tag{7}$$

and

$$T_z = \frac{h\nu_z}{k_{\mathrm{B}} \ln(A_{\mathrm{BSB}}/A_{\mathrm{RSB}})}. \tag{8}$$

For the ensemble cooled by ARP, the sideband measurement is repeated independently 20 times. Each spectrum is analyzed separately, and the reported values are the means of the repeated measurements. The quoted uncertainties are the corresponding standard errors of the means. Before sideband cooling, the axial temperature is 1.8 μK, with $p_0 = 0.79$. Continuous fixed frequency sideband cooling gives $T_z = 1.2$ μK and $p_0 = 0.91$. After ten ARP cooling cycles, we obtain $T_z = 0.86(9)$ μK, $\bar{n}_z = 0.038(13)$, and $p_0 = 0.963(13)$.

4. Conclusion

We have investigated ARP on the clock transition of a one-dimensional ^{87}Sr optical lattice clock, with emphasis on its application to motional sidebands and axial sideband cooling. The carrier excitation was first characterized and then used as a reference for studying sideband ARP, where the resonance frequency and Rabi coupling depend on the motional state. A mode-resolved calculation was developed to describe this dependence and was tested against the measured blue-sideband dynamics.

On the carrier transition, ARP reached a maximum excitation fraction of 0.98(2), compared with 0.76(1) obtained by fixed-frequency Rabi driving under the same experimental conditions. On the blue sideband, ARP increased the maximum excitation fraction from 0.47(2) to 0.55(3), and the measured sweep duration dependence was reproduced by the mode-resolved calculation. The calculation indicates that the present blue-sideband transfer is mainly limited by the finite sideband Rabi frequency relative to the sweep bandwidth, and predicts that the transfer efficiency can exceed 0.88 when the carrier Rabi frequency is increased to 15 kHz. Applying red-sideband ARP to axial sideband cooling reduced the mean axial vibrational occupation to $\bar{n}_z = 0.038$, corresponding to a motional ground-state population of $p_0 = 0.96$.

These results show that ARP on motional sidebands in lattice-trapped atoms cannot be described by directly extending the carrier ARP picture, as the resonance frequency and Rabi coupling vary with the motional state. The model and measurements provide quantitative guidance for optimizing sweep parameters and Rabi frequencies in sideband excitation and cooling. The predicted improvement of blue-sideband transfer at higher Rabi frequencies remains to be tested experimentally. Future work can combine stronger clock-transition coupling with optimized sweep parameters, lower radial temperatures, and improved sideband coherence. Extending ARP cooling to the radial motion may enable more complete motional-state control in lattice-trapped atoms.

Appendix A Theory of carrier excitation

Appendix A.1 Effective Rabi frequency on the carrier transition

In this Appendix we derive the effective Rabi frequency for the carrier transition of the lattice-trapped atoms. The derivation follows the standard treatment of Rabi spectroscopy in a one-dimensional optical

lattice clock, where the electronic clock transition is coupled to the quantized external motion through the spatial phase of the probe field. We denote the two clock states by

$$|g\rangle \equiv |^1S_0\rangle, \qquad |e\rangle \equiv |^3P_0\rangle. \tag{9}$$

Near the magic wavelength, the two clock states experience nearly identical trapping potentials. Therefore, to leading order, the motional eigenstates can be taken to be common for $|g\rangle$ and $|e\rangle$.

At a lattice depth of 73.5 E_r, the motion in a single lattice site is well approximated by a harmonic oscillator along the lattice axis and a weak harmonic oscillator in the radial direction, with small corrections from the axial anharmonicity and the Gaussian radial profile of the lattice beam. We denote the axial motional quantum number by n_z, and group the two radial quantum numbers into

$$n_r = n_x + n_y, \tag{10}$$

which has degeneracy n_r+1. Keeping the leading axial anharmonicity and the leading axial-radial coupling, the motional energy is written as

$$\begin{aligned} E_{n_z,n_r} = {} & h\nu_z\left(n_z+\frac{1}{2}\right) + h\nu_r\left(n_r+1\right) \\ & - \frac{h\nu_\mathrm{rec}}{2}\left(n_z^2+n_z+\frac{1}{2}\right) - h\nu_\mathrm{rec}\frac{\nu_r}{\nu_z}\left(n_z+\frac{1}{2}\right)\left(n_r+1\right), \end{aligned} \tag{11}$$

where ν_z and ν_r are the axial and radial trap frequencies, and

$$\nu_\mathrm{rec} = \frac{E_\mathrm{rec}}{h} \tag{12}$$

is the lattice recoil frequency. The first two terms in Eq. (11) are the harmonic axial and radial energies. The last two terms give the leading corrections from the axial lattice anharmonicity and the coupling between the axial and radial motions. These corrections are essential for determining the sideband resonance frequencies derived below, which depend on the motional state. For the carrier transition, where the motional quantum numbers are unchanged, they do not shift the transition frequency at the magic wavelength, but they define the common motional basis used throughout the carrier and sideband calculations.

The clock laser is described by a plane wave with wave vector $\mathbf{k}_p$. In the electric dipole approximation for this weak clock transition, the atom-laser interaction contains the spatial phase factor $\exp(i\mathbf{k}_p\cdot\hat{\mathbf{r}})$. After transforming to the frame rotating at the probe frequency and applying the rotating wave approximation, the interaction Hamiltonian can be written as

$$\hat{H}_\mathrm{int} = -\frac{\hbar\delta}{2}\hat{\sigma}_z + \frac{\hbar\Omega_0}{2}\left[e^{i\mathbf{k}_p\cdot\hat{\mathbf{r}}}|e\rangle\langle g| + e^{-i\mathbf{k}_p\cdot\hat{\mathbf{r}}}|g\rangle\langle e|\right], \tag{13}$$

where $\delta = \omega_p - \omega_0$ is the detuning of the clock laser from the unperturbed clock transition, Ω_0 is the bare Rabi frequency of a free atom at the same probe intensity, and $\hat{\sigma}_z = |e\rangle\langle e| - |g\rangle\langle g|$.

The coupling between two motional states $|\mathbf{n}\rangle$ and $|\mathbf{n}'\rangle$ is therefore

$$\Omega_{\mathbf{n}',\mathbf{n}} = \Omega_0\langle\mathbf{n}'|e^{i\mathbf{k}_p\cdot\hat{\mathbf{r}}}|\mathbf{n}\rangle. \tag{14}$$

Since the harmonic oscillator wave functions are separable, the matrix element factorizes into the spatial directions,

$$\Omega_{\mathbf{n}',\mathbf{n}} = \Omega_0\prod_\mu\langle n'_\mu|e^{ik_\mu\hat{r}_\mu}|n_\mu\rangle, \tag{15}$$

where k_μ is the projection of the wave vector of the clock laser along direction μ.

For a harmonic oscillator,

$$\hat{r}_\mu = r_{0,\mu}\left(\hat{a}_\mu + \hat{a}_\mu^\dagger\right), \qquad r_{0,\mu} = \sqrt{\frac{\hbar}{2m\omega_\mu}}, \tag{16}$$

where $\omega_\mu = 2\pi\nu_\mu$. We define the Lamb-Dicke parameter

$$\eta_\mu = k_\mu r_{0,\mu} = k_\mu\sqrt{\frac{\hbar}{2m\omega_\mu}}. \tag{17}$$

Using the Baker–Campbell–Hausdorff relation,

$$e^{i\eta(\hat{a}+\hat{a}^\dagger)} = e^{-\eta^2/2}e^{i\eta\hat{a}^\dagger}e^{i\eta\hat{a}}, \tag{18}$$

one obtains, for $n' \geq n$,

$$\langle n'|e^{i\eta(\hat{a}+\hat{a}^\dagger)}|n\rangle = e^{-\eta^2/2}(i\eta)^{n'-n}\sqrt{\frac{n!}{n'!}}L_n^{n'-n}(\eta^2), \tag{19}$$

where $L_n^\alpha(x)$ is a generalized Laguerre polynomial. The corresponding expression for $n' < n$ is obtained by taking the Hermitian-conjugate matrix element.

The carrier transition preserves the motional quantum numbers. Therefore, Eq. (19) reduces to

$$\langle n|e^{i\eta(\hat{a}+\hat{a}^\dagger)}|n\rangle = e^{-\eta^2/2}L_n(\eta^2). \tag{20}$$

For the calculations resolved by motional mode below, we write the carrier Rabi frequency as

$$\Omega_{\mathrm{c}}(n_z, n_r) = \Omega_0 e^{-(\eta_z^2+\eta_r^2)/2}L_{n_z}(\eta_z^2)L_{n_r}(\eta_r^2) \tag{21}$$

where

$$\eta_z = k_z\sqrt{\frac{\hbar}{2m\omega_z}}, \qquad \eta_r = k_r\sqrt{\frac{\hbar}{2m\omega_r}}. \tag{22}$$

For a nearly axial clock beam with a small misalignment angle θ,

$$k_z \simeq k_p\cos\theta, \qquad k_r \simeq k_p\sin\theta, \qquad k_p = \frac{2\pi}{\lambda_p}. \tag{23}$$

Equation (21) is the carrier coupling used to describe excitation inhomogeneity in the atomic ensemble.

In the Lamb-Dicke regime, $\eta_\mu \ll 1$, one may expand

$$e^{-\eta_\mu^2/2}L_{n_\mu}(\eta_\mu^2) = 1 - \left(n_\mu + \frac{1}{2}\right)\eta_\mu^2 + O(\eta_\mu^4). \tag{24}$$

Thus the carrier Rabi frequency is approximately

$$\Omega_{\mathrm{c}}(n_z, n_r) \simeq \Omega_0\left[1 - \left(n_z + \frac{1}{2}\right)\eta_z^2 - \left(n_r + \frac{1}{2}\right)\eta_r^2\right]. \tag{25}$$

Equation (25) shows explicitly that occupation of higher motional states reduces the carrier coupling and produces a distribution of Rabi frequencies.

For a single atom in motional state (n_z, n_r), the carrier excitation probability after a square pulse of duration t is

$$P^{\mathrm{c}}_{e,n_z,n_r}(t,\delta) = \frac{\Omega_{\mathrm{c}}^2(n_z,n_r)}{\Omega_{\mathrm{c}}^2(n_z,n_r)+\delta^2}\sin^2\left[\frac{t}{2}\sqrt{\Omega_{\mathrm{c}}^2(n_z,n_r)+\delta^2}\right]. \tag{26}$$

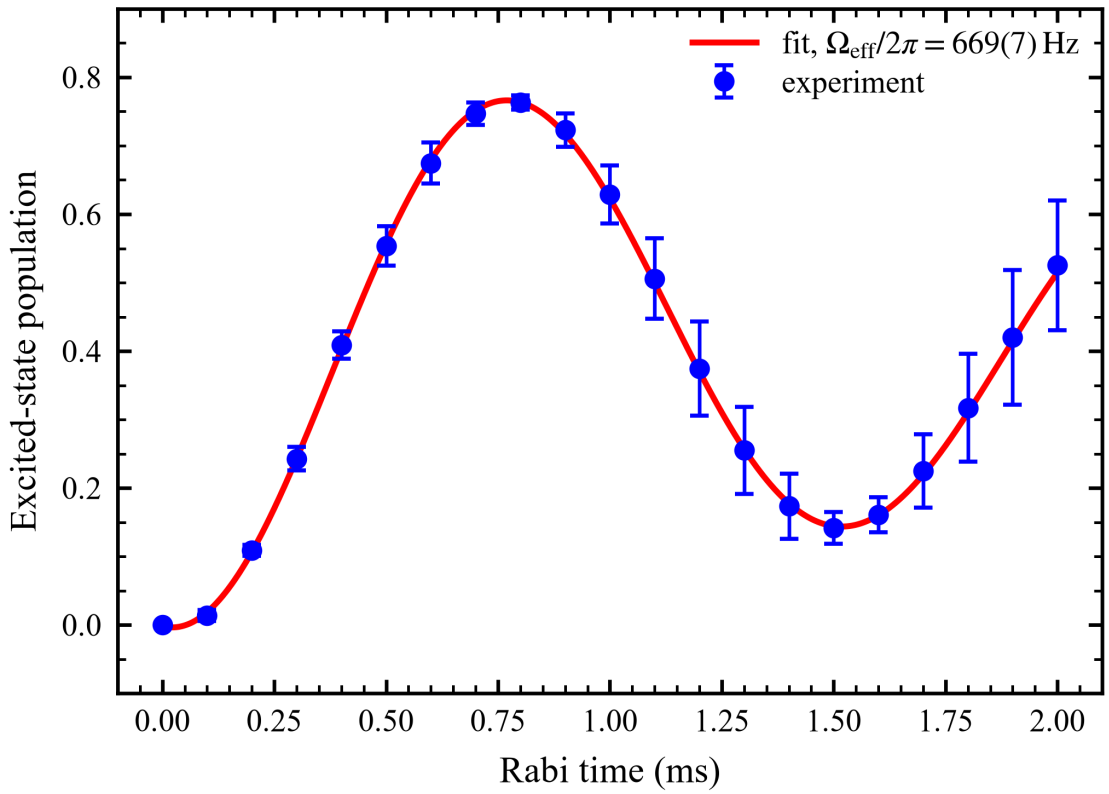


Fig. 7. The excitation under fixed-frequency Rabi driving. The solid line denotes the fit curve. The errors of the measured data in the figure originate from fluctuations in the clock laser power and the atom number. Error bars denote the standard error of the mean from 20 measurements.

For an ensemble with a thermal motional distribution, the carrier excitation probability is obtained by averaging Eq. (26) over all occupied motional states,

$$P_e^{\rm c}(t,\delta) = \sum_{n_z,n_r} W_{n_z,n_r} P^{\rm c}_{e,n_z,n_r}(t,\delta). \tag{27}$$

The normalized thermal weight used in the calculation is

$$W_{n_z,n_r} = \frac{q_z^{n_z}(n_r+1)q_r^{n_r}}{\sum_{n_z,n_r} q_z^{n_z}(n_r+1)q_r^{n_r}}, \tag{28}$$

with

$$q_z = \exp\left(-\frac{h\nu_z}{k_{\rm B}T_z}\right), \qquad q_r = \exp\left(-\frac{h\nu_r}{k_{\rm B}T_r}\right). \tag{29}$$

The zero-point energies do not appear in Eq. (28), because they contribute only an overall Boltzmann factor that cancels in the normalized distribution. The factor $n_r + 1$ accounts for the degeneracy of the two-dimensional radial harmonic oscillator.

Equations (21)–(27) provide the microscopic description of carrier Rabi excitation in the lattice. Experimentally, the full thermal average in Eq. (27) can be replaced by a compact phenomenological fit when the goal is to extract a single observable ensemble Rabi frequency. On resonance, the measured Rabi oscillation is fitted by

$$P_e(t) = C + \frac{A}{2}\left[1 - e^{-\gamma t}\cos(\Omega_{\rm eff}t + \phi)\right] \tag{30}$$

Here Ω_{eff} is the fitted effective carrier Rabi frequency, A is the oscillation amplitude, γ is a phenomenological damping rate, ϕ is the oscillation phase and C is an offset accounting for residual background and imperfect normalization. The damping term represents the combined effect of inhomogeneity in the Rabi frequency, residual dephasing, and technical fluctuations during the measurement. This fitting function is the form used for the carrier Rabi-oscillation data in this work.

Using the measured carrier Rabi oscillation from Fig. 7 and the fitting model in Eq. (30), we obtain $\Omega_{\text{eff}}/2\pi = 669(7)$ Hz. The fitted damping rate is consistent with zero within the uncertainty for the present short-time data window. Therefore, for the ARP and sideband measurements discussed in the main text, we take $\Omega_{\text{eff}}/2\pi = 669(7)$ Hz as the experimentally calibrated effective carrier Rabi frequency.

Appendix A.2 Carrier ARP with effective relaxation and dephasing

We next discuss the calculation of the carrier adiabatic rapid passage (ARP) efficiency in the presence of finite coherence and population relaxation. The carrier ARP is used to transfer population between the two clock states without changing the motional quantum number,

$$|g, n_z\rangle \leftrightarrow |e, n_z\rangle. \tag{31}$$

For a given motional state, and after applying the rotating-wave approximation, the driven two-level Hamiltonian can be written as

$$\hat{H}_{\text{ARP}}(t) = \frac{\hbar}{2}\begin{pmatrix} -\delta(t) & \Omega_{\text{eff}} \\ \Omega_{\text{eff}} & \delta(t) \end{pmatrix}, \tag{32}$$

where Ω_{eff} is the effective carrier Rabi frequency calibrated experimentally and $\delta(t)$ is the time-dependent detuning of the clock laser. For a linear frequency sweep across the carrier resonance, we take the following

$$\delta(t) = v\left(t - \frac{T_{\text{sw}}}{2}\right), \tag{33}$$

where T_{sw} is the total sweep duration and

$$v = \left|\frac{d\delta}{dt}\right| = \frac{2\pi\Delta f_{\text{sw}}}{T_{\text{sw}}} \tag{34}$$

is the angular sweep rate. Here Δf_{sw} denotes the total sweep range in Hz. In the ideal coherent limit, the probability for adiabatic transfer through a single avoided crossing is given by the Landau-Zener expression

$$P_{\text{LZ}}^{(0)} = 1 - \exp\left(-\frac{\pi\Omega_{\text{eff}}^2}{2v}\right). \tag{35}$$

This formula captures the basic behavior of ARP. A slower sweep rate v or a larger Rabi frequency Ω_{eff} makes the evolution more adiabatic and causes the transfer probability to approach unity. [36,37]

However, in the experiment, the ARP process is not perfectly coherent. The finite linewidth of the clock laser, residual magnetic-field fluctuations, inhomogeneous light shifts, Rabi-frequency inhomogeneity, and motional-state averaging all reduce the contrast of the driven dynamics. We account for these effects phenomenologically by introducing an effective Ramsey coherence time T_2, which is determined independently from the decay of Ramsey contrast in the main text. It is important to emphasize that T_2 is an effective ensemble coherence time, rather than a microscopic homogeneous transverse relaxation time. In the present ARP calculation, its effect is included through a dimensionless reduction factor

$$\eta_2 = \frac{1}{1 + 1/(\Omega_{\text{eff}} T_2)}. \tag{36}$$

The Landau-Zener exponent is then modified as

$$P_{\mathrm{LZ}} = 1 - \exp\left(-\frac{\pi\Omega_{\mathrm{eff}}^2\eta_2}{2v}\right). \tag{37}$$

This expression should be regarded as an effective description of dephasing during the ARP pulse. In the limit $\Omega_{\mathrm{eff}}T_2 \gg 1$, one obtains $\eta_2 \simeq 1$, and the coherent Landau-Zener result in Eq. (35) is recovered.

In addition to transverse dephasing, the final population measured after the ARP pulse can be reduced by longitudinal relaxation and loss processes. In an open two-level system, the parameter T_1 usually denotes the relaxation time of the population inversion, or equivalently the decay time scale of the diagonal components of the density matrix toward their values of the steady state. In the present carrier ARP measurement, however, the relevant relaxation is not restricted to the intrinsic natural decay of the $^3P_0$ clock state. The measured transfer efficiency may also be affected by lattice-induced scattering, residual atom loss, off-resonant excitation, imperfect state preparation or detection, and technical fluctuations during the frequency sweep. We therefore introduce an effective longitudinal relaxation time, denoted by T_1, to characterize the net population survival during the ARP pulse.

This effective parameter should not be interpreted as a direct measurement of the natural lifetime of the clock excited state. Rather, it is a phenomenological time scale that summarizes all processes that reduce the detectable transferred population during the chirped interrogation. Since these processes are not independently resolved in the present measurement, T_1 is treated as a fit parameter. The simplest way to include this effect is to multiply the coherent Landau-Zener transfer probability by an exponential survival factor,

$$S(T_{\mathrm{sw}}) = \exp\left(-\frac{T_{\mathrm{sw}}}{2T_1}\right). \tag{38}$$

Equivalently, the factor $1/(2T_1)$ may be viewed as an effective loss rate for the measured ARP transfer probability within this phenomenological model. This convention is used only to parametrize the observed reduction of the final excitation probability at long sweep durations. Combining Eqs. (37) and (38), the final carrier ARP transfer probability is modeled as

$$P_{\mathrm{ARP}}(T_{\mathrm{sw}}) = \left[1 - \exp\left(-\frac{\pi\Omega_{\mathrm{eff}}^2\eta_2}{2v}\right)\right]\exp\left(-\frac{T_{\mathrm{sw}}}{2T_1}\right), \tag{39}$$

with

$$v = \frac{2\pi\Delta f_{\mathrm{sw}}}{T_{\mathrm{sw}}}, \qquad \eta_2 = \frac{1}{1 + 1/(\Omega_{\mathrm{eff}}T_2)}. \tag{40}$$

The physical content of Eq. (39) is transparent. For very short sweep durations, the sweep rate v is large and the passage is nonadiabatic, so the Landau-Zener transfer probability is small. As T_{sw} increases, v decreases and the transfer becomes increasingly adiabatic. At even longer sweep durations, however, the finite relaxation time of the population produces a slow reduction through the survival factor. The measured ARP efficiency is therefore determined by the competition between improved adiabaticity and accumulated relaxation.

In the fit, we fix the independently measured effective Ramsey coherence time to $T_2 = 275$ ms. The carrier Rabi frequency and sweep range are fixed to $\Omega_{\mathrm{eff}}/2\pi = 669$ Hz and $\Delta f_{\mathrm{sw}} = 12$ kHz, respectively. The only free physical parameter is then T_1. We determine it by minimizing the sum of squared residuals

$$\chi^2(T_1) = \sum_i \left[P_{\mathrm{ARP}}(T_i; T_1, T_2) - P_i^{\mathrm{exp}}\right]^2, \tag{41}$$

where P_i^{exp} is the measured final excited state probability for sweep duration T_i. In practice, we perform a grid search over $0.2\ \mathrm{s} \le T_1 \le 20\ \mathrm{s}$. The vertical scale is fixed to unity, so the fitted curve directly represents the calculated transfer probability without introducing an additional normalization factor.

The best fit gives $T_1 = 0.702$ s, with a root-mean-square residual of approximately RMSE $= 3.9\times10^{-2}$. Because the fit is performed without assigning experimental uncertainties to each data point, the extracted value of T_1 should be interpreted as an effective model parameter rather than a direct lifetime measurement. The result indicates that the carrier ARP data are consistent with a survival time on the order of one second under the present interrogation conditions.

We stress that T_1 and T_2 have different meanings. The parameter T_2 is fixed by an independent Ramsey coherence measurement and characterizes the loss of phase coherence of the ensemble. By contrast, T_1 is extracted from the ARP transfer curve and characterizes the effective loss of detectable population during the ARP pulse. Therefore, T_1 should not be interpreted as the intrinsic natural lifetime of the $^3P_0$ clock state. It is a phenomenological longitudinal relaxation time that includes both physical population loss and technical imperfections relevant to the ARP process.

Appendix B Theory of the Blue Sideband

Appendix B.1 Motional sideband spectrum and the effective blue sideband Rabi frequency

We now discuss the motional sideband spectrum and the calibration of the blue sideband Rabi frequency. The motional energies, thermal weights, and matrix elements for atom light coupling have been introduced in Sec. Appendix A.1. Therefore, we only summarize the parts that are specific to sideband excitation.

The carrier transition preserves the motional state,

$$|g, n_z, n_r\rangle \to |e, n_z, n_r\rangle. \tag{42}$$

In contrast, the longitudinal blue and red sidebands change the axial motional quantum number by $+1$ and -1, respectively:

$$\text{blue sideband}: \qquad |g, n_z, n_r\rangle \to |e, n_z + 1, n_r\rangle, \tag{43}$$

$$\text{red sideband}: \qquad |g, n_z, n_r\rangle \to |e, n_z - 1, n_r\rangle. \tag{44}$$

The blue sideband lies at higher probe frequency than the carrier, because the clock excitation is accompanied by the creation of one axial vibrational quantum. The red sideband lies at lower probe frequency, because one axial vibrational quantum is annihilated. Since the red sideband is absent for atoms in $n_z = 0$, the asymmetry between the red and blue sidebands provides a probe of the axial motional temperature.

Using the motional energy in Eq. (11), the detuning of the longitudinal blue sideband from the carrier is

$$\begin{aligned}\gamma_{\mathrm{b}}(n_z, n_r) &= \frac{E_{n_z+1,n_r} - E_{n_z,n_r}}{h} \\ &= \nu_z - \nu_{\mathrm{rec}}(n_z + 1) - \nu_{\mathrm{rec}}\frac{\nu_r}{\nu_z}(n_r + 1),\end{aligned} \tag{45}$$

and the corresponding red sideband detuning is

$$\begin{aligned}\gamma_{\mathrm{r}}(n_z, n_r) &= \frac{E_{n_z-1,n_r} - E_{n_z,n_r}}{h} \\ &= -\nu_z + \nu_{\mathrm{rec}} n_z + \nu_{\mathrm{rec}}\frac{\nu_r}{\nu_z}(n_r + 1), \qquad n_z \geq 1.\end{aligned} \tag{46}$$

In the harmonic limit, the sidebands would be located at $\pm\nu_z$. The axial anharmonicity and axial-radial coupling make the sideband frequencies depend on n_z and n_r, so the observed sideband spectrum is a thermal average over many slightly shifted resonances.

The Rabi matrix element on the blue sideband follows directly from Eq. (19). For the axial blue sideband, the axial quantum number changes as $n_z \to n_z + 1$, while the radial quantum number is unchanged. Therefore, using the same Lamb-Dicke parameters as in Eq. (17), the mode-dependent blue sideband Rabi frequency is

$$\Omega_{\mathrm{b}}(n_z, n_r) = \Omega_0 e^{-(\eta_z^2+\eta_r^2)/2} \frac{\eta_z}{\sqrt{n_z+1}} L^1_{n_z}(\eta_z^2) L_{n_r}(\eta_r^2). \tag{47}$$

The phase factor i associated with the sideband matrix element has been omitted, since only the magnitude of the Rabi frequency enters the excitation dynamics.

Equation (47) shows that the coupling on the blue sideband is suppressed relative to the carrier by approximately the Lamb-Dicke factor η_z. In the Lamb-Dicke limit and for low axial excitation,

$$\Omega_{\mathrm{b}}(0, n_r) \simeq \eta_z \Omega_{\mathrm{c}}(0, n_r). \tag{48}$$

This reflects the usual sideband suppression of the Rabi coupling, because the sideband transition requires a change in motional state and is therefore weaker than the carrier transition.

The experimentally measured carrier Rabi frequency is the effective ensemble carrier frequency, not the bare coupling Ω_0. Therefore, before calculating the sideband Rabi frequency, we first infer the bare Rabi frequency from the carrier calibration. From Eq. (21), the carrier reduction factor is

$$\mathcal{C}_{\mathrm{c}} = \sum_{n_z, n_r} W_{n_z,n_r} e^{-(\eta_z^2+\eta_r^2)/2} L_{n_z}(\eta_z^2) L_{n_r}(\eta_r^2). \tag{49}$$

Thus,

$$\Omega_0 = \frac{\Omega_{\mathrm{c}}^{\mathrm{eff}}}{\mathcal{C}_{\mathrm{c}}}. \tag{50}$$

Here $\Omega_{\mathrm{c}}^{\mathrm{eff}}$ is the experimentally calibrated carrier Rabi frequency obtained in Sec. Appendix A.1. This procedure provides an in situ calibration of the actual coupling strength between the atom and the light field at the position of the atomic sample.

After Ω_0 is determined from the carrier, the blue sideband coupling for each motional component is calculated from Eq. (47). Since the atomic ensemble contains many motional states, a single Rabi frequency on the blue sideband is only an effective characterization. We define the thermally averaged root mean square Rabi frequency on the blue sideband as

$$\Omega_{\mathrm{b}}^{\mathrm{eff}} = \left[\sum_{n_z, n_r} W_{n_z,n_r} \left| \Omega_{\mathrm{b}}(n_z, n_r) \right|^2 \right]^{1/2}. \tag{51}$$

Combining Eqs. (47), (49), and (50), we obtain

$$\Omega_{\mathrm{b}}^{\mathrm{eff}} = \Omega_{\mathrm{c}}^{\mathrm{eff}} \frac{\left[\sum_{n_z, n_r} W_{n_z,n_r} \left| e^{-(\eta_z^2+\eta_r^2)/2} \frac{\eta_z}{\sqrt{n_z+1}} L^1_{n_z}(\eta_z^2) L_{n_r}(\eta_r^2) \right|^2 \right]^{1/2}}{\sum_{n_z, n_r} W_{n_z,n_r} e^{-(\eta_z^2+\eta_r^2)/2} L_{n_z}(\eta_z^2) L_{n_r}(\eta_r^2)}. \tag{52}$$

Equation (52) summarizes the calibration procedure used in this work, where the measured carrier Rabi oscillation first determines the bare atom-light coupling, and this calibrated coupling is then inserted into the sideband matrix element to obtain the blue sideband coupling scale.

For the blue sideband Rabi measurement at a fixed frequency, the dynamics is not reduced to the scalar value $\Omega_{\mathrm{b}}^{\mathrm{eff}}$. Instead, each thermally occupied component is propagated with its own $\Omega_{\mathrm{b}}(n_z, n_r)$ and its own detuning from the applied drive frequency. For a drive frequency f_{d}, the angular detuning of mode (n_z, n_r) is

$$\Delta_{n_z,n_r} = 2\pi \left[f_{\mathrm{d}} - \gamma_{\mathrm{b}}(n_z, n_r) \right]. \tag{53}$$

The corresponding two-level Hamiltonian is

$$\hat{H}_{n_z,n_r} = \frac{\hbar}{2} \left[\Omega_{\mathrm{b}}(n_z, n_r)\hat{\sigma}_x + \Delta_{n_z,n_r}\hat{\sigma}_z \right], \tag{54}$$

where the Rabi frequency and detuning are both expressed as angular frequencies. The calculated excitation probability is then thermally averaged over W_{n_z,n_r}. This full calculation resolved by motional mode naturally includes the inhomogeneous broadening of the blue sideband due to the spread of $\gamma_{\mathrm{b}}(n_z, n_r)$, as well as the motional dependence of the sideband Rabi coupling.

Appendix B.2 Mode-resolved simulation of blue sideband pulse excitation

Having obtained the thermal weights W_{n_z,n_r}, the mode-dependent blue sideband resonance frequencies $\gamma_{\mathrm{b}}(n_z, n_r)$, and the calibrated blue sideband Rabi frequencies $\Omega_{\mathrm{b}}(n_z, n_r)$ in the previous subsection, we now describe how the blue sideband pulse excitation is calculated. The purpose of this calculation is not to approximate the ensemble by a single effective two-level system, but to propagate each thermally occupied motional component separately and then perform the thermal average at the end. This procedure is necessary because different motional components are driven with different detunings and different Rabi frequencies.

For a fixed probe frequency f_{d}, each motional component

$$j \equiv (n_z, n_r)$$

is modeled as an independent two-level system formed by

$$|g, n_z, n_r\rangle \quad \text{and} \quad |e, n_z + 1, n_r\rangle.$$

In the rotating frame of the probe field, the Hamiltonian for this component is

$$\hat{H}_j = \frac{\hbar}{2} \left[\Omega_j \hat{\sigma}_x + \Delta_j \hat{\sigma}_z \right], \tag{55}$$

where

$$\Omega_j = 2\pi\Omega_{\mathrm{b}}(n_z, n_r), \tag{56}$$

and

$$\Delta_j = 2\pi \left[f_{\mathrm{d}} - \gamma_{\mathrm{b}}(n_z, n_r) \right]. \tag{57}$$

Here $\Omega_{\mathrm{b}}(n_z, n_r)$ is expressed in Hz before the factor 2π is applied. The detuning Δ_j includes the motional dependence of the blue sideband resonance frequency. Thus, even for a single fixed probe frequency, the ensemble contains a distribution of effective detunings.

The density matrix of each motional component is initialized as

$$\rho_j(0) = |g\rangle\langle g| = \begin{pmatrix} 1 & 0 \\ 0 & 0 \end{pmatrix}. \tag{58}$$

For a short time step Δt, the coherent part of the evolution is generated by

$$\rho_j(t+\Delta t) = \hat{U}_j(\Delta t)\rho_j(t)\hat{U}_j^\dagger(\Delta t), \tag{59}$$

where

$$\hat{U}_j(\Delta t) = \exp\left[-\frac{i}{\hbar}\hat{H}_j\Delta t\right]. \tag{60}$$

Defining the generalized Rabi frequency

$$\Omega_{R,j} = \sqrt{\Omega_j^2 + \Delta_j^2}, \tag{61}$$

the propagator can be written explicitly as

$$\hat{U}_j(\Delta t) = \cos\left(\frac{\Omega_{R,j}\Delta t}{2}\right)\hat{I} - i\sin\left(\frac{\Omega_{R,j}\Delta t}{2}\right)\left(\frac{\Omega_j}{\Omega_{R,j}}\hat{\sigma}_x + \frac{\Delta_j}{\Omega_{R,j}}\hat{\sigma}_z\right). \tag{62}$$

In the $\{|g\rangle, |e\rangle\}$ basis, this propagator has the matrix form

$$\hat{U}_j = \begin{pmatrix} a_j & b_j \\ b_j & d_j \end{pmatrix}, \tag{63}$$

with

$$a_j = c_j - is_j\frac{\Delta_j}{\Omega_{R,j}}, \tag{64}$$

$$b_j = -is_j\frac{\Omega_j}{\Omega_{R,j}}, \tag{65}$$

$$d_j = c_j + is_j\frac{\Delta_j}{\Omega_{R,j}}, \tag{66}$$

where

$$c_j = \cos\left(\frac{\Omega_{R,j}\Delta t}{2}\right), \qquad s_j = \sin\left(\frac{\Omega_{R,j}\Delta t}{2}\right). \tag{67}$$

Writing the density matrix as

$$\rho_j = \begin{pmatrix} \rho_{gg}^{(j)} & \rho_{ge}^{(j)} \\ \rho_{eg}^{(j)} & \rho_{ee}^{(j)} \end{pmatrix}, \tag{68}$$

Eq. (59) gives the explicit update equations

$$\rho_{gg}^{(j)\prime} = |a_j|^2\rho_{gg}^{(j)} + a_jb_j^*\rho_{ge}^{(j)} + b_ja_j^*\rho_{eg}^{(j)} + |b_j|^2\rho_{ee}^{(j)}, \tag{69}$$

$$\rho_{ee}^{(j)\prime} = |b_j|^2\rho_{gg}^{(j)} + b_jd_j^*\rho_{ge}^{(j)} + d_jb_j^*\rho_{eg}^{(j)} + |d_j|^2\rho_{ee}^{(j)}, \tag{70}$$

$$\rho_{ge}^{(j)\prime} = a_jb_j^*\rho_{gg}^{(j)} + a_jd_j^*\rho_{ge}^{(j)} + |b_j|^2\rho_{eg}^{(j)} + b_jd_j^*\rho_{ee}^{(j)}. \tag{71}$$

The element $\rho_{eg}^{(j)\prime}$ is obtained from Hermiticity,

$$\rho_{eg}^{(j)\prime} = \left[\rho_{ge}^{(j)\prime}\right]^*.$$

The long blue sideband pulse is also affected by loss of optical coherence. Instead of introducing a microscopic model for each possible noise source, we include this effect phenomenologically by applying a pure-dephasing step to the off-diagonal density-matrix elements after each coherent update:

$$\rho_{ge}^{(j)}(t+\Delta t) \to \rho_{ge}^{(j)}(t+\Delta t)\exp\left(-\frac{\Delta t}{T_{\mathrm{BSB}}}\right), \tag{72}$$

and

$$\rho_{eg}^{(j)}(t+\Delta t) \to \rho_{eg}^{(j)}(t+\Delta t)\exp\left(-\frac{\Delta t}{T_{\mathrm{BSB}}}\right). \tag{73}$$

Here T_{BSB} denotes the effective blue sideband coherence-decay time. We use the symbol T_{BSB} rather than T_2 to distinguish this fitted sideband damping time from the Ramsey coherence time discussed for the carrier. Physically, T_{BSB} summarizes the loss of phase coherence during the sideband pulse applied at a fixed frequency, including residual probe-frequency noise, unresolved motional inhomogeneity, imperfect knowledge of the sideband resonance distribution, and other technical dephasing effects. In the present calculation, no longitudinal population relaxation is included; the diagonal populations are modified only through the coherent drive.

Equations (59)–(72) are iterated up to the desired pulse time. The physical excitation probability before detection correction is then obtained by thermally averaging the excited state populations of all motional components,

$$P_{\mathrm{th}}(t;T_{\mathrm{BSB}}) = \sum_{n_z,n_r} W_{n_z,n_r}\rho_{ee}^{(n_z,n_r)}(t;T_{\mathrm{BSB}}). \tag{74}$$

This expression contains both the coherent Rabi dynamics of each mode and the dephasing-induced damping of the ensemble-averaged sideband excitation.

To compare the calculated excitation probability with the measured signal, we use the experimentally calibrated detection model

$$P_{\mathrm{obs}}(t;T_{\mathrm{BSB}}) = P_{\mathrm{bg}} + \mathcal{A}P_{\mathrm{th}}(t;T_{\mathrm{BSB}}), \tag{75}$$

where P_{bg} is the independently measured background offset and $\mathcal{A}$ is the independently measured detection normalization factor. These two quantities are fixed by the experimental calibration and are not treated as physical fit parameters in the sideband dynamics. Therefore the only free dynamical parameter in the blue sideband pulse model is T_{BSB}.

The value of T_{BSB} is obtained by minimizing the least-squares residual between the measured pulse-excitation data and the calculated curve,

$$\chi^2(T_{\mathrm{BSB}}) = \sum_i \left[P_{\mathrm{obs}}(t_i;T_{\mathrm{BSB}}) - P_i^{\mathrm{exp}}\right]^2. \tag{76}$$

Equivalently, the fitting procedure determines the sideband coherence decay time that best reproduces the damping and saturation behavior of the measured pulse excitation on the blue sideband at a fixed frequency. The resulting T_{BSB} should therefore be interpreted as an effective damping time for the blue sideband excitation model, rather than as an independently measured carrier Ramsey coherence time.

Appendix B.3 Numerical calculation of blue sideband ARP

We finally describe the calculation of adiabatic rapid passage on the blue sideband. The calculation uses the same sideband model resolved by motional mode established in Sec. Appendix B.2. In particular, the thermal weights W_{n_z,n_r}, the blue sideband resonance frequencies $\gamma_{\mathrm{b}}(n_z,n_r)$, and the calibrated blue sideband Rabi frequencies $\Omega_{\mathrm{b}}(n_z,n_r)$ are kept fixed. The effective sideband coherence-decay time T_{BSB}, the background offset P_{bg}, and the detection normalization factor $\mathcal{A}$ are also inherited from the fixed-frequency blue sideband pulse calibration. Thus the ARP calculation introduces no additional dynamical fit parameter; it provides a direct prediction based on the calibrated sideband model.

For each motional component $j \equiv (n_z,n_r)$, we use the same two-level subspace as in the fixed-frequency blue sideband calculation,

$$|g,n_z,n_r\rangle \quad \text{and} \quad |e,n_z+1,n_r\rangle.$$

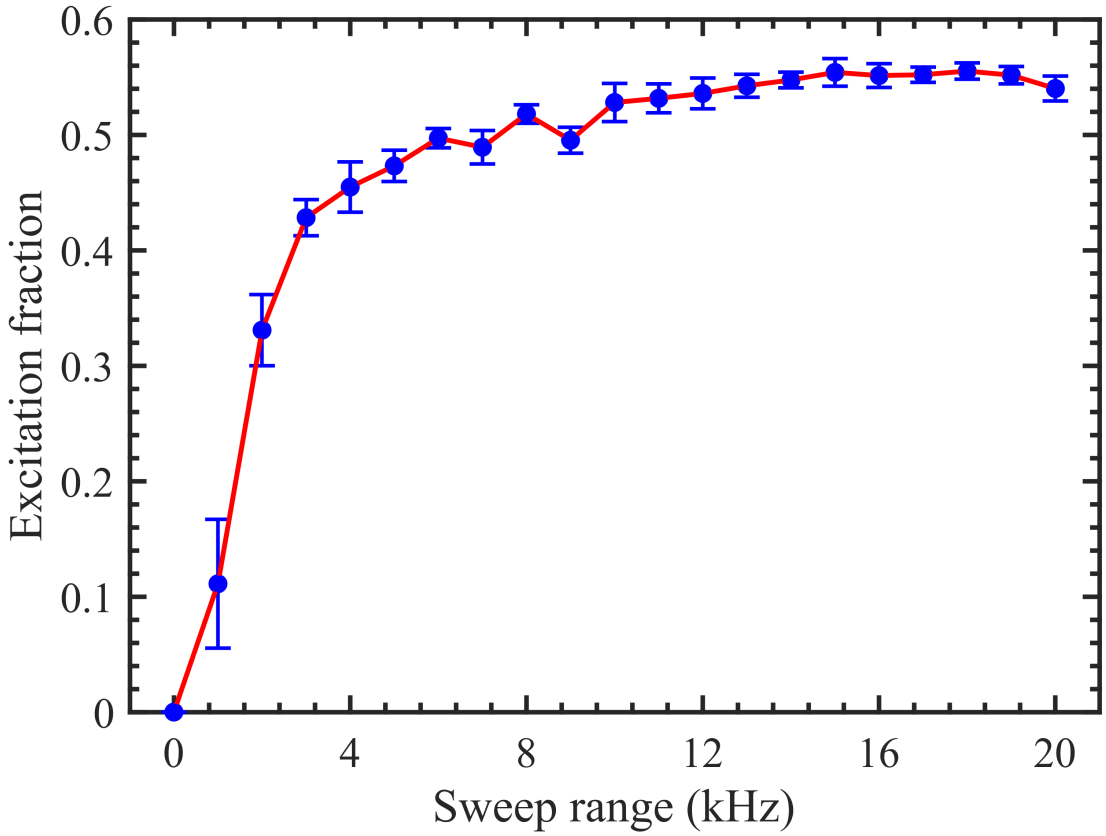


Fig. 8. Final excited-state fraction as a function of sweep span at $T_{\rm sw} = 270$ ms.The initial frequency is fixed at the blue-sideband corner frequency, while the final frequency is moved toward the carrier. Error bars denote the standard error of the mean from 20 measurements.

The only change is that the probe frequency is swept in time. We take a linear chirp,

$$f(t) = f_{\rm i} + \frac{f_{\rm f} - f_{\rm i}}{T_{\rm sw}} t, \qquad 0 \le t \le T_{\rm sw}, \tag{77}$$

where $T_{\rm sw}$ is the sweep duration. For the sweep from high frequency to low frequency used here,

$$f_{\rm i} = f_{\rm c} + \frac{\Delta f_{\rm sw}}{2}, \qquad f_{\rm f} = f_{\rm c} - \frac{\Delta f_{\rm sw}}{2}, \tag{78}$$

with $f_{\rm c}$ the sweep center and $\Delta f_{\rm sw}$ the total sweep span. The instantaneous detuning for mode j is therefore

$$\Delta_j(t) = 2\pi \left[f(t) - \gamma_{\rm b}(n_z, n_r) \right]. \tag{79}$$

Different motional components consequently cross resonance at different times during the same sweep.

To determine the sweep span for blue-sideband ARP, we measure the final excited-state fraction as a function of $\Delta f_{\rm sw}$ at a fixed sweep duration of $T_{\rm sw} = 270$ ms. The initial frequency is fixed at the blue-sideband corner frequency, while the final frequency is moved toward the carrier as the sweep span is increased. As shown in Fig. 8, the excitation fraction increases with the sweep span and reaches a plateau at approximately 15 kHz. We therefore select $\Delta f_{\rm sw} = 15$ kHz for blue-sideband ARP.

The Hamiltonian and short-time density-matrix propagation are evaluated using the same expressions as Eqs. (55)–(62), with the replacement

$$\Delta_j \to \Delta_j(t).$$

The coupling

$$\Omega_j = 2\pi\Omega_{\rm b}(n_z, n_r)$$

is kept constant during the square-amplitude ARP pulse, while the detuning is updated according to Eq. (79).

For a given sweep duration $T_{\rm sw}$, the time interval is divided into $N_{\rm step}$ steps with

$$\Delta t = \frac{T_{\rm sw}}{N_{\rm step}}. \tag{80}$$

At the ℓ-th step, the detuning is evaluated at the midpoint

$$t_\ell = \left(\ell + \frac{1}{2}\right)\Delta t, \qquad \ell = 0, 1, \ldots, N_{\rm step} - 1. \tag{81}$$

This midpoint prescription approximates the evolution in time order by a product of propagators over short time intervals with Hamiltonians that are constant on each time step. Explicitly, for each step we use the fixed-frequency propagator of Eq. (62), evaluated with $\Delta_j(t_\ell)$ and

$$\Omega_{R,j}(t_\ell) = \sqrt{\Omega_j^2 + \Delta_j^2(t_\ell)}. \tag{82}$$

The density matrix is then updated according to Eq. (59).

The initial state of each motional component is

$$\rho_j(0) = |g\rangle\langle g|. \tag{83}$$

After each coherent update, the same phenomenological pure dephasing operation as in Eq. (72) is applied to the off diagonal elements of the density matrix. The dephasing time is fixed to the value $T_{\rm BSB}$ obtained from the fixed-frequency sideband-pulse calibration. No additional longitudinal relaxation process is included in the blue sideband ARP calculation.

The full evolution of mode j may therefore be viewed as a time-ordered sequence of coherent updates interleaved with the same dephasing map used in the pulse calculation,

$$\rho_j(T_{\rm sw}) = \prod_{\ell=0}^{N_{\rm step}-1} \left[\mathcal{D}_{T_{\rm BSB}}\mathcal{U}_{j,\ell}\right] \rho_j(0), \tag{84}$$

where the product is ordered from early to late times,

$$\mathcal{U}_{j,\ell}\rho = \hat{U}_{j,\ell}\rho\hat{U}_{j,\ell}^\dagger,$$

and $\mathcal{D}_{T_{\rm BSB}}$ denotes the dephasing map defined in Eq. (72).

After the sweep, the physical ARP excitation probability is obtained by thermally averaging the final excited state populations,

$$P_{\rm ARP}^{\rm th}(T_{\rm sw}) = \sum_{n_z,n_r} W_{n_z,n_r}\rho_{ee}^{(n_z,n_r)}(T_{\rm sw}). \tag{85}$$

This thermal average includes the distribution of resonance-crossing times and Rabi frequencies over the occupied motional components. The calculated ARP transfer efficiency is therefore not described by a single Landau-Zener crossing, but by a mode-resolved average over many passages.

Finally, the same detection model used for the fixed-frequency sideband pulse is applied,

$$P_{\rm ARP}^{\rm obs}(T_{\rm sw}) = P_{\rm bg} + \mathcal{A}P_{\rm ARP}^{\rm th}(T_{\rm sw}). \tag{86}$$

Here P_{bg} and $\mathcal{A}$ are fixed by the independent detection calibration and are not refitted. For comparison with experiment, the calculation is repeated for the measured sweep durations T_{sw}, while a denser set of T_{sw} values is used to generate the smooth theoretical curve. Agreement between $P_{\mathrm{ARP}}^{\mathrm{obs}}(T_{\mathrm{sw}})$ and the measured ARP transfer curve therefore tests whether the same calibrated sideband Hamiltonian, motional distribution, and coherence decay time consistently describe both sideband excitation at a fixed frequency and ARP transfer.

Data availability

Data supporting the findings of this study are available from the corresponding authors upon reasonable request.

Acknowledgements

This work is supported by the National Natural Science Foundation of China (Grant Nos. 62405327), the Key Research and Development Projects of Shaanxi Province (No. 2025CY-YBXM015), and the Innovation Program for Quantum Science and Technology (Grant No. 2021ZD0300902).

References

[1] Aeppli A, Kim K, Warfield W, Safronova M S and Ye J 2024 *Phys. Rev. Lett.* **133** 023401

[2] Hassan Y S, Beloy K, Siegel J L, Kobayashi T, Swiler E, Grogan T, Brown R C, Rojo T, Bothwell T, Hunt B D, Halaoui A and Ludlow A D 2025 *Phys. Rev. Lett.* **135** 063402

[3] Liu X Y, Liu P, Li J, Wang Y B, Jia Z P, Zhang X, Zhu X Q, Kong D Q, Song W L, Niu G Z, Yang Y M, Feng P J, Liu X P, Cui X Y, Xu P, Jiang X, Yin J, Liao S K, Dai H N, Chen Y A and Pan J W 2025 *Phys. Rev. Lett.* **135** 263402

[4] Lu X T, Guo F, Liu Y Y, Cao J, Li J A, Xia J J, Xu Q F, Lu B Q, Wang Y B and Chang H 2025 *Metrologia* **62** 035007

[5] Filzinger M, Doerscher S, Lange R, Klose J, Steinel M, Benkler E, Peik E, Lisdat C and Huntemann N 2023 *Phys. Rev. Lett.* **130** 253001

[6] Gotti I, Condio S, Clivati C, Risaro M, Gozzelino M, Costanzo G A, Levi F, Calonico D and Pizzocaro M 2023 *Metrologia* **60** 035002

[7] Lu X T, Guo F, Wang Y B, Xu Q F, Zhou C H, Xia J J, Wu W J and Chang H 2023 *Metrologia* **60** 015008

[8] Safronova M S, Porsev S G, Sanner C and Ye J 2018 *Phys. Rev. Lett.* **120** 173001

[9] Bothwell T, Kennedy C J, Aeppli A, Kedar D, Robinson J M, Oelker E, Staron A and Ye J 2022 *Nature* **602** 420

[10] Grotti J, Koller S, Vogt S, Haefner S, Sterr U, Lisdat C, Denker H, Voigt C, Timmen L, Rolland A, Baynes F N, Margolis H S, Zampaolo M, Thoumany P, Pizzocaro M, Rauf B, Bregolin F, Tampellini A, Barbieri P, Zucco M, Costanzo G A, Clivati C, Levi F and Calonico D 2018 *Nat. Phys.* **14** 437

[11] Takamoto M, Ushijima I, Ohmae N, Yahagi T, Kokado K, Shinkai H and Katori H 2020 *Nat. Photonics* **14** 411

[12] Zheng X, Dolde J, Cambria M C, Lim H M and Kolkowitz S 2023 *Nat. Commun.* **14** 4886

[13] Goepfert A, Bloch I, Haubrich D, Lison F, Schütze R, Wynands R and Meschede D 1997 *Phys. Rev. A* **56** R3354

[14] Warren W S, Bates J L, McCoy M A, Navratil M and Mueller L 1986 *J. Opt. Soc. Am. B* **3** 488

[15] Whitley R M and Stroud C R 1976 *Phys. Rev. A* **14** 1498

[16] Bartolotta J P and Holland M J 2020 *Phys. Rev. A* **101** 053434

[17] Bartolotta J P, Norcia M A, Cline J R K, Thompson J K and Holland M J 2018 *Phys. Rev. A* **98** 023404

[18] Loy M M T 1974 *Phys. Rev. Lett.* **32** 814

[19] Norcia M A, Cline J R K, Bartolotta J P, Holland M J and Thompson J K 2018 *New J. Phys.* **20** 023021

[20] Yatsenko L P, Guerin S and Jauslin H R 2002 *Phys. Rev. A* **65** 043407

[21] Camparo J C and Frueholz R P 1984 *Phys. Rev. A* **30** 803

[22] Mitra A, Martin M J, Biedermann G W, Marino A M, Poggi P M and Deutsch I H 2020 *Phys. Rev. A* **101** 030301

[23] Vitanov N V, Halfmann T, Shore B W and Bergmann K 2001 *Annu. Rev. Phys. Chem.* **52** 763

[24] Abragam A 1961 *The Principles of Nuclear Magnetism* (Oxford: Clarendon Press)

[25] Beterov I I, Tretyakov D B, Entin V M, Yakshina E A, Ryabtsev I I, Saffron M and Bergamini S 2020 *J. Phys. B* **53** 184005

[26] Lambert J, Noel M W and Gallagher T F 2002 *Phys. Rev. A* **66** 053413

[27] Maeda H, Gurian J H, Norum D V L and Gallagher T F 2006 *Phys. Rev. Lett.* **96** 073002

[28] Xu S J, Li X W, Li X L, Li J B and Xue M 2024 *Phys. Rev. A* **110** 023108

[29] Hobson R, Bowden W, Vianello A, Hill I R and Gill P 2020 *Phys. Rev. A* **101** 013420

[30] Siegel J L, McGrew W F, Hassan Y S, Chen C C, Beloy K, Grogan T, Zhang X and Ludlow A D 2024 *Phys. Rev. Lett.* **132** 133201

[31] Xie X P, Zhuang W and Chen J B 2010 *Chin. Phys. Lett.* **27** 074202

[32] Kim K, Aeppli A, Warfield W, Chu A J, Rey A M and Ye J 2025 *Phys. Rev. Lett.* **135** 103601

[33] Blatt S, Thomsen J W, Campbell G K, Ludlow A D, Swallows M D, Martin M J, Boyd M M and Ye J 2009 *Phys. Rev. A* **80** 052703

[34] Xia J J, Guo F, Liu Y Y, Lu X T and Chang H 2025 *Acta Opt. Sin.* **45** 0302001

[35] Chen C C, Siegel J L, Hunt B D, Grogan T, Hassan Y S, Beloy K, Gibble K, Brown R C and Ludlow A D 2024 *Phys. Rev. Lett.* **133** 053401

[36] Hassan Y S, Kobayashi T, Bothwell T, Seigel J L, Hunt B D, Beloy K, Gibble K, Grogan T and Ludlow A D 2024 *Quantum Sci. Technol.* **9** 045023

[37] Bothwell T, Hunt B D, Seigel J L, Hassan Y S, Grogan T, Kobayashi T, Gibble K, Porsev S G, Safronova M S, Brown R C, Beloy K and Ludlow A D 2025 *Phys. Rev. Lett.* **134** 033201